Title

Hyperbolic load-displacement analysis of helical and expanded piles: database approach

Authors

Rahimi, A

Eslami, A

McCartney, JS

Publication Date

2024

DOI

10.1680/jgeen.23.00196

Peer reviewed

Accepted manuscript doi:
10.1680/jgeen.23.00196

Accepted manuscript doi:
10.1680/jgeen.23.00196

Submitted: 20 October 2023

Published online in 'accepted manuscript' format: 15 March 2024

Manuscript title: Hyperbolic load-displacement analysis of helical and expanded piles: database approach

Authors: A. Rahimi[1], A. Eslami[1,2] and J. S. McCartney[3]

Affiliations: [1]Department of Civil and Environmental Engineering, Amirkabir University of Technology, Tehran, Iran; [2]University of California, San Diego, USA and [3]Department of Structural Engineering, University of California, San Diego, USA

Corresponding author: A. Eslami, Department of Civil and Environmental Engineering, Amirkabir University of Technology, Tehran, Iran.

E-mail: afeslami@aut.ac.ir

Accepted manuscript doi:
10.1680/jgeen.23.00196

Abstract

In recent years, there has been a focus on improving geotechnical systems by implementing and constructing new deep foundation such as helical and expanded piles. This study examined the effects of parameters such as embedment depth, pile geometry, and axial loading direction on the load-displacement behaviour of these piles. To conduct the research, a database was compiled consisting of 80 axial loading test records for different piles. The embedment depth of the piles ranged from 2.4 to 36.8 m, and the diameter of helices or expanded parts ranged from 254 to 1500 mm. The ultimate load of the piles was determined using the 2.5% and 5% displacement ratio criteria and the Brinch-Hansen 80% method. Additionally, hyperbolic functions were fitted to the load-displacement curves, allowing for consistent estimation of the limit load and the initial tangent modulus. Analysis of the results from the database revealed that the dominant factors influencing the ultimate load, limit load, maximum measured load, initial stiffness, and load-displacement behaviour were the ratio of helices or expanded part diameter to shaft diameter, shaft and toe surface area, and load direction. Correlations derived from the database were validated using measurements from eight full-scale helical and expanded piles.

Keywords: Load-displacement; Helical and expanded piles; Database; Hyperbolic function analysis; Ultimate load

Accepted manuscript doi:
10.1680/jgeen.23.00196

Introduction

In recent years, new pile design and installation techniques such as helical piles and expanded piles have emerged, offering potential benefits in terms of increased construction productivity and speed (e.g., Li et al., 2018a). Understanding the factors affecting the load-displacement curves is crucial for determining the ultimate load and bearing capacity of these piles. Therefore, investigating the factors that influence this behaviour can aid in the design of these piles and the development of new ones.

To reduce uncertainties and facilitate statistical analyses in geotechnical practice, it is common to utilize correlations from databases (Moshfeghi & Eslami, 2018a). Databases are helpful tools in terms of time and cost to formulate more optimum designs (Shirani et al., 2023). For instance, Abu-Farsakh and Titi (2004) conducted a study on 35 prestressed concrete piles (PPC) to evaluate eight different methods for determining bearing capacity based on cone penetration test (CPT) results. Similarly, Eslami and Fellenius (1997) compiled a database consisting of static load test results from 102 piles and CPT data from 40 sites across 13 countries to investigate methods for estimating bearing capacity based on CPT and CPTu. Schneider et al. (2008) examined the performance of various methods for estimating bearing capacity using CPT tests on 77 piles from a larger set of 200 piles tested by the University of Western Australia. (Van Dijk & Kolk, 2011) developed a method for determining the bearing capacity of marine piles using a database of 33 steel pipe piles from 15 different locations. Mandolini and Di Laora (2019) also furnish experimental support for the design of axially-loaded piles. Experimental data consist of nearly 400 full-scale pile load tests. More recently, Moshfeghi and Eslami (2018b) collected load-displacement curves and CPT data from 47 sources spanning 23 countries. Based on these studies, creating a comprehensive database of expanded and helical piles could serve as a valuable tool for further investigation in this field.

In this study, a comprehensive database has been created, which includes information on the location and soil type, as well as the geometric characteristics of the pile and load-displacement curve. In the beginning and a conventional survey, the values of the ultimate load have been calculated and examined using several different methods. Additionally, the hyperbolic function was fitted to the load-displacement curves. The hyperbolic model provides a consistent approach to estimate the limit load and initial stiffness, which can also be used to develop correlations with pile characteristics. Finally, correlations obtained from the database analysis were validated using 8 independent tests on different piles.

2. Background

Engineers have used helical piles as an approach to augment the geometry of piles and change the load-displacement curve for more than 170 years (Lutenegger, 2013). However, there are other types of expanded piles that have been proposed to reach similar goals, as shown in Figure 1. Belled piles have been used since the 1930’s and are among the piles that increase the bearing capacity by

changing the body geometry. The cone placed at the end of these piles increases their tensile and compressive load capacity (Harris & Madabhushi, 2015). Squeezed-branch piles are a new generation of belled piles that, in addition to the geometry, their execution method has changed. These piles can have one or more expanded parts in their body. By better load distribution in the soil, these parts enhance the piles bearing capacity under tensile and compressive loads. Expandable body technology has been another example of efforts to increase the bearing capacity of piles (Cui & Wang, 2012; Piao & Qu, 2012). This method was successfully used for small in-situ piles in loose and dense soils. The expandable body system consists of a folded steel opening section attached to the pile toe, and when the pile is installed, the folded steel expands with grout injection (Terceros Arce & Terceros Herrera, 2016). For example, a new type of pile is the x-section-in-place concrete (XCC) pile, whose body shape was developed to reduce soil displacement caused by liquefaction (Li et al., 2018b). This pile has been widely used in China for land improvement (Liu et al., 2014; Zhou et al., 2017) and the foundation of structures (Lv et al., 2012; Zhang et al., 2015). Pulse Discharge Technology (PDT) has also been used to increase the pile capacity by changing the shape of the pile. It improves the frictional resistance, compacting the soil by changing the pile shape and the well wall (Dzhantimirov et al., 2005; Kang, 2009). Drilled-Displacement (DD) piles are another type of piles that show a behavior between drilled and driven piles (Basu et al., 2014). They are becoming more popular due to the lack of noise and vibration during installation, good resistance of concrete against corrosion, and good compatibility with coastal environments (Basu et al. 2014; Moshfeghi & Eslami, 2018a).

(Shojaei et al., 2021) introduced the concept of self-expanded piles. In this type of pile, the execution method and geometry of the pile have been changed. The use of driven piles with a variable cross-section and minimal disturbance in the upper layers of the soil could be the starting point for the invention and application of self-expanding piles. These piles are designed to expand their expansion part in a suitable layer of soil and provide the necessary capacity. Reduced installation effects in this type of pile have increased its bearing capacity. These pile types were introduced under three titles: bubble piles, wing piles, and self-expanded piles (Shojaei et al., 2021). Helical piles are also one of the known pile types that can be considered similar to this category of piles. Since about 1836, helical piles have been used successfully as spiral foundations around the world to support a variety of structures (Lutenegger, 2013). The application of helical piles in marine sites has been addressed by Ebrahimipour and Eslami (2024). These piles are shown in Figure 2.

3. Database

Predicting the ultimate axial loading of the piles in Figures 1 and 2 can be quite complex due to the presence of the helices or expanded parts of the pile that induce different amounts of disturbance during installation. A database of the helical and expanded pile axial loading test results was collected to investigate the load-displacement behaviour. Specifically, 158 full-scale and 149 small-scale piles

were collected and analysed by Rahimi and Eslami (2022). By removing the small-scale piles as well as repetitive tests at the same time of full-scale piles in a given location, 80 piles were selected to form the database for helical and expanded piles evaluated in this study. The collected data includes geometrical characteristics, soil profile, and load-displacement curves. The facts and features of these piles are presented in Table 1. Selected piles include 53 helical piles and 27 expanded piles. The collected data were from 5 countries and 27 sites, 23 cases from China, 2 cases from Ireland, 6 cases from the United States, 34 cases from Canada, and 15 cases from Brazil. 43 cases were under compressive loading, and 37 cases were under tensile loading. The embedment depth of these cases ranged from 2.4 to 36.8 meters. The general information on the cases is presented in Table 2. Examples of the load-displacement curves for selected piles are shown in Figure 3 to highlight the detail of the soil layering and pile geometry that accompanies the load-displacement curve.

4. Ultimate Load: Conventional Criterion and Assessment

The ultimate load was determined using both the 2.5% and 5% displacement ratio criteria. The displacement ratio is calculated by dividing the displacement of the pile head by the average diameter of the helices or expanded sections. Additionally, the Brinch-Hansen 80% method was also used to estimate the ultimate load. This method involves determining the load for which the displacement exceeds four times the value measured after 80% of the load has been applied Hansen (1963), Fellenius (2001). The 10% displacement ratio criterion was also considered, but it was not used due to the large values of helices and expanded diameters in many of the cases considered, which resulted in the displacement not reaching 10% of the mean of helices or expanded parts diameter. Figure 6 shows the load vs. displacement ratio curves for these cases.

In certain instances, it was not feasible to calculate the ultimate load using all methods due to the shape of the load-displacement curves. Consequently, the ultimate load was determined by prioritizing the Brinch-Hansen 80% method and the 5% displacement ratio criterion in order to review and categorize the cases. For the remaining cases, the 2.5% displacement ratio criterion and the maximum measured load were used, respectively. This process is illustrated in Figure 7, which depicts all of the load-displacement curves in the database. The figure (Figure 7) comprises five layers, with the four inner layers representing the 2.5% and 5% criterion, the Brinch-Hansen 80% method, and the method employed to determine the ultimate load for each case, respectively. The outermost layer consists of 80 segments, each representing an item in the database. The case ID of each item is labelled next to it.

According to the ultimate load, the cases were classified into four categories: 0 to 500 kN, 500 to 1000 kN, 1000 to 1500 kN, and more than 1500 kN, and two types of tensile and compressive loading. The load-displacement curves of the items placed in each category are shown in Figure 8.

Accepted manuscript doi:
10.1680/jgeen.23.00196

In the compression tests within the 0 to 500 kN range, cases 156 and 345 displayed the softest and hardest load-displacement curves, respectively. Furthermore, despite cases 128 and 345 having the same maximum measured load, their load-displacement behaviour differed, resulting in a significant difference in their ultimate load. This variation in load-displacement behaviour can be attributed to factors such as variations in geometrical size, embedment depth, and the presence of underground water at the installation location of case 128. Additionally, in the tensile loading, case 333 recorded the highest maximum measured load of 702 kN. This placement is based on the utilization of a 5% criterion for calculating the ultimate load.

In the compression tests in the 500 to 1000 kN range, cases 344 and 130 exhibited the most brittle and ductile load-displacement curves, respectively. Similarly, for tensile loading, cases 362 and 317 displayed the most brittle and ductile curves, respectively.

In the 1000 to 1500 kN category, case 10 exhibited the highest ultimate load in tensile loading. This pile is a bored expanded base pile with an ultimate load that is only 28% more than that of case 341, although its embedment depth is 3.7 times larger. In the compressive loading, case 133 endured the greatest load of 1745 kN out of the cases in this category. This case, as well as case 340, share the same geometry and both employ the 5% criterion to determine the ultimate load. However, despite these similarities, the ultimate load for case 340 is 50% lower than that of case 133. This discrepancy can be attributed to the presence of underground water at the site where case 340 was executed (with a water table depth of 1.2 meters for case 10).

Among the compressive loading cases with an ultimate load greater than 1500 kN, two cases 220 and 137 have the highest and lowest maximum measured loads, respectively. Case 220 with a maximum measured load of 11747 kN carried the highest load among the cases in the database. This pile was an expanded type (squeezed branch pile) with an embedment depth of 17.3 meters. 5 cases in the tensile loading category have an ultimate load of more than 1500 kN, of which one is a helical pile and the other 4 are expanded type piles (belled piles).

To analyse the impact of geometric characteristics on the ultimate load and load-displacement behaviour of all pile cases in the database, scatter diagrams were created to compare parameters such as mean of helices or expanded parts diameter, shaft diameter, and pile embedment depth with the calculated ultimate load. The combined parameters of the toe area, which affects the force mobilized at the pile toe, and the shaft area, which influences shaft friction force, were calculated and examined due to their positive effects. Due to the differences in the geometry of the helical and expanded piles, these parameters have been selected and used based on the similarity in these piles. The fitting equations shown on these graphs are presented in Table 3, whose parameters indicate a positive correlation between increasing values of these parameters and the ultimate load. It is important to note that the data used in the scatter charts were selected based on the feasibility of applying the ultimate

load determination methods mentioned above. However, a significant observation from the results in Table 3 is the positive impact of increasing the surface area at the toe of piles when subjected to tensile loading. This matter will be further explored and discussed.

5. Hyperbolic Function for Load-displacement Analysis

The hypothetical limit load assessed from the shape of the load-displacement curve can be used as an indicator of the load-displacement behaviour. However, piles often do not have a clear value of limit load as the load-displacement curve shows a hardening response with continued displacement. Because of its accurate alignment with load-displacement curves, the hyperbolic function has been effectively employed to determine the limit load and initial stiffness. The general form of the hyperbolic function is given as follows:

$$F = \frac{\delta}{a\delta+b} \qquad 1.$$

To determine the constants *a* and *b*, Equation (1) can be linearized as follows:

$$\frac{1}{F} = \frac{a\delta+b}{\delta} \rightarrow \frac{1}{F} = a + b\frac{1}{\delta} \qquad 2.$$

Equations 3 and 4 demonstrate the relationship between parameters a and b and the limit load and initial stiffness. Specifically, the limit load is equal to the reciprocal of a, while the initial stiffness is equal to the inverse of b.

$$F = \frac{\delta}{a\delta+b} \rightarrow \frac{\delta}{a\delta+b} \times \frac{\frac{1}{\delta}}{\frac{1}{\delta}} = \frac{1}{a+\frac{b}{\delta}} \rightarrow \lim_{\delta \rightarrow \infty} \frac{1}{a+\frac{b}{\delta}} = \frac{1}{a} \qquad 3.$$

the derivation of the function:

$$F = \frac{\delta}{a\delta+b} \rightarrow F' = \frac{b}{b^2+2ab\delta+a^2\delta^2} \rightarrow \lim_{\delta \rightarrow 0} F' = \frac{1}{b} \qquad 4.$$

The displacement at the point where the initial stiffness intersects with the limit load is equivalent to the displacement needed to reach half of the limit load, as follows:

$$if\ b = \frac{\delta}{F_{limit}}\ and\ a = \frac{1}{F_{limit}} \rightarrow F = \frac{\delta}{\frac{\delta}{F_{limit}} + \frac{1}{F_{limit}} \times \delta} = \frac{F_{limit}}{2} \qquad 5.$$

$$\frac{F_{limit}}{2} = \frac{\delta}{a\delta+b} \rightarrow \frac{1}{2a} = \frac{\delta}{a\delta+b} \rightarrow Displacement\ at\ F_{limit}/2 = \frac{b}{a} \qquad 6.$$

This displacement value is equal to the ratio of b to a. To determine the hyperbolic function that best fits the load-displacement curves of helical and expanded piles, the unloading sections should have been removed. The process of calculating these two parameters for case 259 is shown in Figure 9.

To gain a better understanding of the load-displacement behaviour, the load and displacement values were normalized by dividing them by the maximum measured load and the maximum observed displacement, respectively. Subsequently, the normalized curves were fitted with a hyperbolic function. The resulting curves are shown in Figure 10.

Based on Equation 7, we can determine the range of intercept and slope values for the two categories of tensile and compressive cases. Figure 11 displays the fitted line, as well as the 95% prediction and confidence intervals for both categories.

$$\alpha = \frac{\Delta}{a\Delta+b} \rightarrow \frac{\alpha}{\Delta} = \frac{1}{a\Delta+b} \rightarrow \frac{\Delta}{\alpha} = a\Delta + b \qquad 7.$$

Accepted manuscript doi:
10.1680/jgeen.23.00196

The cases were categorized into three groups based on the embedded depth: short (less than 6 meters), semi-deep (6 to 12 meters), and long (12 to 24 meters). Out of the total cases, 35 fell into the short category, 19 into the semi-deep category, and 23 into the long category. Only three cases had an embedment depth greater than 24 meters, so they were not assigned to a separate category. The load-displacement curves for the short, semi-deep, and long categories are shown in Figures 12, 13, and 14, respectively.

- Short Piles

Among the cases in the short category, the highest maximum measured loads were carried by two specific instances: case 343, which was tested in sandy soil and experienced a tensile load of 1793 kN, and case 133, which was tested in fine-grained soil and had a compression load of 1745 kN. The initial stiffness of the cases in this category ranged from 848 to 8 kN/mm, with an average of 210 kN/mm. Figure 12 also shows the points of contact initial stiffness and limit load of the piles. The displacements of these points were all less than 10.6 mm.

- Semi-deep Piles

In the semi-deep category, the highest maximum measured loads were borne by two cases, namely case 362 and case 122, with loads of 980 kN and 2549 kN, respectively. Both cases were implemented in fine-grained soil. The initial stiffness of case 362 was 255 kN/mm, while for case 122 it was 373 kN/mm. The initial stiffness of the cases placed in this category ranged from 397 to 10 kN/mm, with an average of 169 kN/mm. Figure 13 also shows the points of contact initial stiffness and limit load of the piles. The displacements of these points were less than 9.3 mm.

- Long piles

In the long category, the highest maximum measured loads were borne by two cases, namely case 6 and case 220, with loads of 9432 kN and 11747 kN, respectively. Both cases were implemented in fine-grained soil. The initial stiffness of case 6 was 1143 kN/mm, while for case 220 it was 2931 kN/mm. The initial stiffness of the cases placed in this category ranged from 6022 to 20 kN/mm, with an average of 1016 kN/mm. Figure 14 also shows the points of contact initial stiffness and limit load of the piles. The displacements of these points were less than 16.2 mm.

The variation ranges in the constants of the hyperbolic functions that have been fitted to load-displacement curves are shown in Figure 15. Based on this figure (Figure 15), long piles have the widest range of initial stiffness compared to the other two categories. Also, this parameter in the short and semi-depth piles was in the same range.

6. Discussion

- Impact of the loading direction

To examine the variation in load-displacement characteristics between tensile and compressive load scenarios, a total of 26 helical piles were chosen for analysis. Each pair of piles shared the same geometry and location, with the only distinction being the direction of the applied load. Through plotting the load-displacement curves of these piles, three distinct states were identified in their load-displacement behaviour.

- In 3 pairs, the tensile curves were located on top of the compressive curves. The load-displacement curves of these piles are displayed in Figure 16.a.
- In 5 pairs, unlike the first state, the load-displacement curves of the tensile piles were placed under the compressive piles' curves. Their load-displacement curves are displayed in Figure 16.b.
- In 5 pairs, the load-displacement curve of the compressive piles was initially below the tensile piles' curves. In the following, by an increase in displacement, the compressive piles' curves were crossed with tensile piles' curves and placed on top of them. Their load-displacement curves are displayed in Figure 16.c.

It was expected that the tensile loading curves would either coincide with or be lower than the compressive loading curves, as there is no support reaction at the tip of the pile in tensile loading. However, in the first state, the opposite occurred. Furthermore, the third state revealed that for some piles, at the initial loading and small displacements, the tensile load capacity exceeded the compressive load capacity. Further investigation is needed to understand the reasons behind this phenomenon.

- Mean of helices or expanded parts diameter to shaft diameter ratio

In the ongoing investigation of the pile's geometry, the impact of the ratio between the mean of the expanded part or helix diameter and the shaft diameter on the shape of the load-displacement curve was observed. To analyse this effect further, the normalized load-displacement curves have been used. Figure 17 displays the normalized curves for two categories of tensile and compressive loads. These curves were divided into two groups based on the ratio of the expanded part or helix diameter to the shaft diameter: less than 2.5 and more than 2.5. As depicted in the figure (Figure 17), reducing this ratio resulted in an increased initial tangent modulus of the curves.

- Limit load versus Ultimate load and maximum measured load

By comparing the limit load obtained from the hyperbolic approach in each case with the maximum measured load and ultimate load obtained from different methods (eq. 8), a comprehensive understanding of these methods can be achieved. Figure 18.a illustrates the range of changes in the results for each method. The ratio of the maximum measured load to the limit load obtained from the

Accepted manuscript doi:
10.1680/jgeen.23.00196

hyperbolic approach ranged from 0.68 to 1.38. Ratios greater than 1 indicate that the hyperbolic curve is positioned below the natural load-displacement curve of the pile, as the limit load is based on the maximum measured load reached by the hyperbolic curve at infinite displacement. In over 20% of the database, the maximum measured load exceeded 110% of the limit load, as shown in Figure 18.b, along with the corresponding hyperbolic curve. This indicates that the softening part of the natural load-displacement curves has a low but constant slope, resulting in maximum measured load values surpassing the limit load observed in the hyperbolic curve. The constant slope in the softening part of the curves can be considered a characteristic of load-displacement curves for helical and expanded piles, based on the range of maximum measured load to limit load ratio in conventional piles (0.5 to 0.9 (Wong & Duncan, 1974)).

$$y = \frac{Maximum\ measured\ load}{Limit\ load}\ and\ y = \frac{Ultimate\ load}{Limit\ load} \qquad 8.$$

- Comparison

The AUT research team investigated several self-expanded, expanded, and helical piles in two areas of Anzali Port and Inchebron Village. Also, the small-scale samples of these piles have been tested in the laboratory using the FCV-AUT device. Several full-scale tests have been chosen and presented for review and comparison with the database. The specifications of the tested piles are presented in Table 4.

Self-expanded piles were investigated by Shojaei et al. (2022) in the customs area of Bandar Anzali, Caspian Sea southwest shore. This port in the north of Iran is located at a longitude of 49 degrees and 28 minutes and a latitude of 37 degrees and 28 minutes. Much of the soil in this port is very fine sand with silt particles. The pieces of information extracted from three 30-meter boreholes and a CPTu test up to a depth of 24 have been used to determine the stratification and geotechnical characteristics of the local soil. Based on this, the soil of the test site up to the depth of 16 meters was made of SP, SP-SM, and SM. Also, the underground water level during sampling was at a depth of 1.7 meters.

To investigate and compare the performance difference between full-scale helical piles in natural soil, Arabameri and Eslami (2021) installed and examined several helical piles in the western area of Inchebron village. This village is located at a longitude of 54 degrees and 43 minutes and a latitude of 37 degrees and 27 minutes on, the Caspian Sea's southeast shore and in the border area of Iran and Turkmenistan.

Among the tested piles, 4 expanded and 4 helical piles which have been subjected to compressive loading are selected for comparison. The specifications of these piles are presented in Table 4. According to the maximum load of these piles, several cases from the database were selected for comparison. The load-displacement curves, initial tangent modulus, as well as ultimate load to maximum measured load and ultimate capacity ratio, and finally, the fitted hyperbolic curves of tested

piles compared to the selected cases of the database are shown in Figure 19. The initial stiffness compared to the cases with an embedment depth of 0 to 6 meters in the database was placed in the lower quarter.

7. Conclusions

A database containing 80 helical and expanded piles located in coarse- and fine-grained deposits has been compiled to assess the variables affecting their load-displacement behaviour. The cases varied in depth from 2.4 to 36.8 m and had shaft diameters ranging from 73 to 830 mm. The helices and expanded parts diameters ranged from 254 to 1500 mm, with one to five helices or expanded parts in each case. The ultimate load, limit load, initial stiffness, and load-displacement behaviour of these cases were investigated, considering embedment depth, geometry, and loading direction. The hyperbolic relationship was used to assess relevant variables by fitting that to the measured load-displacement curves. Finally, the outcomes were compared to results from piles not included in the database.

The main findings of the investigation are as follows:

- The ultimate loads were calculated using three criteria: Brinch-Hansen 80% and the 5% and 2.5% criterion. The items in the database were divided into four categories based on the results and a preliminary review was done on them. Upon examining the impact of geometry parameters on the ultimate load obtained from these methods, it was observed that increasing the surface area of the shaft and the toe area had a positive effect in all cases. Surprisingly, even in piles subjected to tensile loading, increasing the toe area positively influenced the ultimate load.
- The hyperbolic function was used to fit the load-displacement records for further analysis. As indicated in the mentioned relations, the parameters a and b in the hyperbolic function represent the initial stiffness and limit load in the load-displacement curve, respectively. Therefore, this function was employed to calculate these parameters. Next, the items in the database were categorized based on their embedment depth into three groups: short (0-6 m), semi-depth (6-12 m), and long (12-24 m). The average initial stiffness for these categories was found to be 210, 169, and 1015 kN/mm, respectively. The variation in this parameter was investigated, with the most significant changes observed in piles with embedment depths ranging from 12 to 24 meters.
- In order to investigate the influence of loading direction on load-displacement behaviour further, a comparison was made between 13 pairs of helical piles with identical conditions under both tensile and compressive loading. In certain instances, the tensile loading curve exceeded the compressive loading curve, necessitating further investigation.

- In the subsequent analysis of the effect of pile geometry on the shape of the load-displacement curve, various parameters were examined. One such parameter that impacted the curve's shape was the ratio of the helices or expanded parts diameter to the shaft diameter. To compare and illustrate this phenomenon, the load-displacement curves were normalized to the maximum measured load and maximum displacement achieved. As this ratio decreased, the initial stiffness of the curves increased and their movement aligned more closely with the load axis.
- The study examined the ratio of the maximum measured load and ultimate load obtained from various methods to the limit load obtained from the hyperbolic approach. The findings showed that there is a significant increase in capacity in the softening area of the curves for expanded and helical piles. This increase is responsible for ratios greater than one when comparing the maximum measured load with the limit load.
- Finally, for comparison and validation, 8 compressive piles were selected from among the tests on several helical and expanded piles performed in Caspian Sea shoreline sites. The load-displacement curve of these piles as well as the initial stiffness and limit loads obtained from hyperbolic function approach analyses were in good agreement with the results obtained from the studied database.

List of notations

F Applied load
δ Pile head displacement
α Normalized applied load
Δ Normalized pile head displacement

References

Abu-Farsakh, M.Y. and Titi, H.H. (2004) Assessment of Direct Cone Penetration Test Methods for Predicting the Ultimate Capacity of Friction Driven Piles. Journal of Geotechnical and Geoenvironmental Engineering 130(9): 935–944, https://doi.org/10.1061/(ASCE)1090-0241(2004)130:9(935).

Arabameri, M. and Eslami, A. (2021) Microstructure and Strength Effect on Bearing Capacity of Helical Piles Installed in Golestan Loess. International Journal of Civil Engineering 19(8): 923–940, https://doi.org/10.1007/S40999-021-00602-2/FIGURES/18.

Basu, P., Prezzi, M., and Basu, D. (2014) Drilled Displacement Piles – Current Practice and Design. DFI Journal-The Journal of the Deep Foundations Institute 4(1): 3–20, https://doi.org/10.1179/DFI.2010.001.

Basu, P., Prezzi, M., and Salgado, R. (2014) Modeling of Installation and Quantification of Shaft Resistance of Drilled-Displacement Piles in Sand. International Journal of Geomechanics 14(2): 214–229, https://doi.org/10.1061/(ASCE)GM.1943-5622.0000303.

Beim, J. and Luna, S.C. (2012) Results of Dynamic and Static Load Tests on Helical Piles in the varved clay of Massachusetts. DFI Journal - The Journal of the Deep Foundations Institute 6(1): 58–67, https://doi.org/10.1179/dfi.2012.005.

Cui, W. and Wang, Z. (2012) Field experiment study on the bearing characteristics of squeezed branch pile in loess area. Applied Mechanics and Materials, 166–169, 1329–1332, https://doi.org/10.4028/www.scientific.net/AMM.166-169.1329.

Dehong, W., Yanzhong, J., Xiaopan, Z., and Junfeng, B. (2017) Field test and numerical simulation on bearing capacity of squeezed branch pile in transmission line. Mechanika, 23(5): 762–768, https://doi.org/10.5755/j01.mech.23.5.19357.

Van Dijk, B.F.J. and Kolk, H.J. (2011) CPT-based design method for axial capacity of offshore piles in clays. In *Frontiers in Offshore Geotechnics II - Proceedings of the 2nd International Symposium on Frontiers in Offshore Geotechnics*, 555–560, https://doi.org/10.1201/B10132-76/CPT-BASED-DESIGN-METHOD-AXIAL-CAPACITY-OFFSHORE-PILES-CLAYS-VAN-DIJK-KOLK.

Dzhantimirov, K.A., Krastelev, E.G., Kryuchkov, S.A., Nistratov, V.M., and Smirnov, P. v. (2005) Geotechnical Technology Based on Electrochemical Explosion and Equipment for Its Implementation. Soil Mechanics and Foundation Engineering 42(5): 172–177, https://doi.org/10.1007/S11204-006-0004-8.

Ebrahimipour, A., & Eslami, A. (2024) Analytical study of piles behavior for marine challenging substructures. Ocean Engineering, 292, 116514. https://doi.org/10.1016/j.oceaneng.2023.116514

Elkasabgy, M. and Naggar, M.H. el (2015) Axial compressive response of large-capacity helical and driven steel piles in cohesive soil. Canadian Geotechnical Journal 52(2): 224–243, https://doi.org/10.1139/cgj-2012-0331.

Elsherbiny, Z. and el Naggar, M.H. (2013) The performance of helical pile groups under compressive loads: A numerical investigation. *In 18th International Conference on Soil Mechanics and Geotechnical Engineering: Challenges and Innovations in Geotechnics, ICSMGE 2013* 4(3): 2723–2726.

Eslami, A. and Fellenius, B.H. (1997) Pile capacity by direct CPT and CPTu methods applied to 102 case histories. Canadian Geotechnical Journal 34(6): 886–904, https://doi.org/10.1139/T97-056/ASSET/T97-056.FP.PNG_V03.

Fahmy, A. and el Naggar, M.H. (2017) Axial Performance of Helical Tapered Piles in Sand. Geotechnical and Geological Engineering 35(4): 1549–1576, https://doi.org/10.1007/s10706-017-0192-1.

Fellenius, B.H. (2001) What capacity value to choose from the results a static loading test. Deep Foundation Institute, Fulcrum: 19-22.

Gao, X.J., Wang, J.C., and Zhu, X.R. (2007) Static load test and load transfer mechanism study of squeezed branch and plate pile in collapsible loess foundation. Journal of Zhejiang University: Science A 8(7): 1110–1117, https://doi.org/10.1631/jzus.2007.A1110.

Gavin, K., Doherty, P., and Tolooiyan, A. (2014) Field investigation of the axial resistance of helical piles in dense sand. Canadian Geotechnical Journal 51(11): 1343–1354, https://doi.org/10.1139/cgj-2012-0463.

Hansen, J.B. (1963) Discussion of "Hyperbolic Stress-Strain Response: Cohesive Soils". Journal of the Soil Mechanics and Foundations Division 89(4), https://doi.org/10.1061/jsfeaq.0000542.

Harris, D.E. and Phani Madabhushi, G.S. (2015) Uplift capacity of an under-reamed pile foundation. https://doi.org/10.1680/jgeen.14.00154 168(6): 526–538, https://doi.org/10.1680/JGEEN.14.00154.

Kang, K.-S.J.-H.G.-Y.T.-H.S.-J. (2009) A Case Study of Applicability of Machines of Pulse Powered Underreamed Anchors. Proceedings of the Korean Geotechnical Society Conference 1100–1106.

Li, W., Chen, Y., Stuedlein, A.W., Liu, H., Zhang, X., and Yang, Y. (2018a) Performance of X-shaped and circular pile-improved ground subject to liquefaction-induced lateral spreading. Soil Dynamics and Earthquake Engineering 109: 273–281, https://doi.org/10.1016/j.soildyn.2018.03.022.

Li, W., Chen, Y., Stuedlein, A.W., Liu, H., Zhang, X., and Yang, Y. (2018b) Performance of X-shaped and circular pile-improved ground subject to liquefaction-induced lateral spreading. Soil Dynamics and Earthquake Engineering 109: 273–281, https://doi.org/10.1016/J.SOILDYN.2018.03.022.

Liu, H., Zhou, H., and Kong, G. (2014) XCC pile installation effect in soft soil ground: A simplified analytical model. Computers and Geotechnics 62: 268–282, https://doi.org/10.1016/J.COMPGEO.2014.07.007.

Lutenegger, A.J. (2013) Historical Development of Iron Screw-Pile Foundations: 1836–1900. The International Journal for the History of Engineering & Technology 81(1): 108–128, https://doi.org/10.1179/175812109X12547332391989.

Lv, Y., Liu, H., Ding, X., and Kong, G. (2012) Field Tests on Bearing Characteristics of X-Section Pile Composite Foundation. Journal of Performance of Constructed Facilities 26(2): 180–189, https://doi.org/10.1061/(ASCE)CF.1943-5509.0000247.

Mandolini A., Di Laora R. (2019) Design of Axially-loaded Piles: Experimental Evidence from 400 Field Tests. Geotechnical Engineering 50(3): 99-105.

Monteiro, F.F., da Cunha, R.P., de Aguiar, M.F.P., and Silva, C.M. (2021) Settlement of bored piles with expander body system in lateritic soils. REM - International Engineering Journal 74(3): 309–318, https://doi.org/10.1590/0370-44672020740057.

Moshfeghi, S. and Eslami, A. (2018a) Reliability-based assessment of drilled displacement piles bearing capacity using CPT records. Marine Georesources & Geotechnology 37(1): 67–80, https://doi.org/10.1080/1064119X.2018.1448493.

Moshfeghi, S. and Eslami, A. (2018b) Study on pile ultimate capacity criteria and CPT-based direct methods. International Journal of Geotechnical Engineering 12(1): 28–39, https://doi.org/10.1080/19386362.2016.1244150.

Piao, C. and Qu, Y. (2012) Study on the bearing mechanism of squeezed branch pile based on BOTDR. Advanced Materials Research 368–373, 2065–2070, https://doi.org/10.4028/www.scientific.net/AMR.368-373.2065.

Rahimi, A.H. and Eslami, A. (2022) Load-Displacement Analysis of Different Expanded Pile for Using in Marine Structures.

Sakr, M. (2009) Performance of helical piles in oil sand. Canadian Geotechnical Journal 46(9): 1046–1061, https://doi.org/10.1139/T09-044.

Sakr, M. (2013) Comparison between high strain dynamic and static load tests of helical piles in cohesive soils. Soil Dynamics and Earthquake Engineering 54: 20–30, https://doi.org/10.1016/j.soildyn.2013.07.010.

Dos Santos Filho, J.M.S.M. and Cavalcanti Tsuha, C. de H. (2019) Uplift performance of helical piles with cement injection in residual soils. Canadian Geotechnical Journal 57(9): 1335–1355, https://doi.org/10.1139/CGJ-2019-0317.

Schneider, J.A., Xu, X., and Lehane, B.M. (2008) Database Assessment of CPT-Based Design Methods for Axial Capacity of Driven Piles in Siliceous Sands. Journal of Geotechnical and Geoenvironmental Engineering 134(9): 1227–1244, https://doi.org/10.1061/(ASCE)1090-0241(2008)134:9(1227).

Shirani, S.S., Eslami, A., Ebrahimipour, A., & Karakouzian, M. (2023) Dominant factors in MiniCone, CPT and pile correlations: a data-based approach. Deep Undergr Sci Eng. 1-13. doi:10.1002/dug2.12055

Shojaei, E., Eslami, A., and Ganjian, N. (2021) Self-expanded piles: A new approach to unconventional piles development. Marine Georesources and Geotechnology 39(1): 115–128, https://doi.org/10.1080/1064119X.2019.1679924.

Shojaei, E., Eslami, A., Ganjian, N., and Ezzatdust, R. (2022) Field investigation on the performance of different screw piles in sandy soils Case study: Bandar Anzali Coast - Anzali Port. Journal of Structural and Construction Engineering 9(3): 5–20, https://doi.org/10.22065/JSCE.2021.243030.2211.

Tappenden, K.M. (2007) Predicting the Axial Capacity of Screw Piles Installed in Western Canadian Soils. University Of Alberta 1–193, https://era.library.ualberta.ca/files/bv73c235m/4008200.pdf.

Terceros Arce, M. and Terceros Herrera, M.A. (2016) The Use of an Expander Body with Full Displacement Piles in Medium-Dense Sandy Soils. 142–151, https://doi.org/10.1061/9780784480076.017.

Weech, C. and Howie, J.A. (2012) Helical piles in soft sensitive soils –a field study of disturbance effects on pile capacity. VGS Symposium on Soft Ground Engineering (D).

Wong, K.S. and James Michael Duncan (1974) Hyperbolic Stress-Strain Parameters for Nonlinear Finite 355 Element Analyses of Stresses of Stresses and Movements in Soil Masses. Berkeley, California.

Xu, H.F., Yue, Z.Q., and Qian, Q.H. (2009) Predicting uplift resistance of deep piles with enlarged bases. Proceedings of the Institution of Civil Engineers: Geotechnical Engineering 162(4): 225–238, https://doi.org/10.1680/geng.2009.162.4.225.

Yin, L., Fan, X., and Wang, S. (2017) A study on application of squeezed branch pile in clay soil foundation. IOP Conference Series: Earth and Environmental Science 61(1), https://doi.org/10.1088/1755-1315/61/1/012091.

Yu, M., Liu, B., Wang, Q., and Song, Y. (2020) Study on Bearing Capacity of Belled Uplift Piles in Soft Clay Area. Indian Geotechnical Journal 50(5): 848–858, https://doi.org/10.1007/s40098-020-00420-8.

Zhang, D., Lv, Y., Liu, H., and Wang, M. (2015) An analytical solution for load transfer mechanism of XCC pile foundations. Computers and Geotechnics 67: 223–228, https://doi.org/10.1016/J.COMPGEO.2015.03.006.

Zhang, D.J.Y. (1999) Predicting Capacity of Helical Screw Piles in Alberta Soils 1–304.

Zhang, M., Xu, P., Cui, W., and Gao, Y. (2018) Bearing behavior and failure mechanism of squeezed branch piles. Journal of Rock Mechanics and Geotechnical Engineering 10(5): 935–946, https://doi.org/10.1016/j.jrmge.2017.12.010.

Zhou, H., Liu, H., Randolph, M.F., Kong, G., and Cao, Z. (2017) Experimental and analytical study of X-section cast-in-place concrete pile installation effect. nternational Journal of Physical Modelling in Geotechnics 17(2): 103–121, https://doi.org/10.1680/JPHMG.15.00037.

Accepted manuscript doi:
10.1680/jgeen.23.00196

Table 1: Database of load tests on piles in different soil layers.

No	ID#	Country	Soil type	Pile type	Height (m)	NEA	Shaft dia. (mm)	MED (mm)	Load direction	Max. measured load (kN)	Maximum displacement (mm)	Reference
1	2	China	(FG)	Expanded Base	16.00	1	800	1500	(T)	7860	93	(Yu et al. 2020)
2	3	China	(FG)	Expanded Base	16.00	1	800	1500	(T)	7860	95	
3	5	China	(FG)	Expanded Base	22.00	1	850	1500	(T)	8646	90	
4	6	China	(FG)	Expanded Base	22.00	1	850	1500	(T)	9432	86	
5	7	China	(FG)	Expanded Base	18.70	1	500	1200	(T)	840	21	(Xu et al. 2009)
6	8	China	(FG)	Expanded Base	18.70	1	500	1200	(T)	887	33	
7	9	China	(FG)	Expanded Base	18.70	1	500	1200	(T)	806	44	
8	10	China	(FG)	Expanded Base	22.10	1	500	1200	(T)	1289	39	
9	11	China	(FG)	Expanded Base	22.10	1	500	1200	(T)	1179	15	
10	12	China	(FG)	Expanded Base	22.10	1	500	1200	(T)	1280	63	
11	103	Canada	(S)	Helical	5.20	1	178	406	(C)	798	10	(Sakr 2009)
12	104	Canada	(S)	Helical	5.00	2	178	406	(C)	808	9	
13	105	Canada	(S)	Helical	5.10	1	178	406	(T)	792	14	
14	106	Canada	(S)	Helical	5.10	2	178	406	(T)	780	9	
1	1	Ca	(S)	Helical	5.3	1	178	40	(C)	1255	52	

5	09	nada			0			6				
16	110	Canada	(S)	Helical	5.30	2	178	406	(C)	1575	40	
17	111	Canada	(S)	Helical	5.10	1	178	406	(T)	619	43	
18	113	Canada	(S)	Helical	5.20	2	178	406	(T)	973	48	
19	122	Canada	(FG)	Helical	9.00	1	324	762	(C)	2549	36	(Sakr 2013)
20	123	Ireland	(S)	Helical	2.57	1	110	400	(C)	588	69	(Gavin et al. 2014)
21	124	Ireland	(S)	Helical	2.57	1	110	400	(T)	241	72	
22	128	USA	(S)	Helical	2.40	1	150	390	(C)	509	90	(Fahmy & el Naggar 2017)
23	130	USA	(S)	Helical	2.75	1	200	390	(C)	471	52	
24	133	Canada	(FG)	Helical	6.00	2	324	610	(C)	1745	44	(Elkasabgy & Naggar 2015)
25	137	Canada	(FG)	Helical	9.00	1	324	610	(C)	2087	62	
26	140	USA	(FG)	Helical	3.70	3	73	254	(C)	108	15	(Beim & Luna 2012)
27	141	USA	(FG)	Helical	5.50	3	73	254	(C)	46	14	
28	145	USA	(FG)	Helical	5.50	3	73	254	(C)	54	14	
29	146	USA	(FG)	Helical	3.70	3	73	254	(C)	110	14	
30	156	Canada	(FG)	Helical	8.50	5	89	356	(C)	63	90	(Weech & Howie 2012)
31	206	China	(FG)	Expanded Body	24.00	3	620	1333	(C)	3897	38	(Gao et al. 2007)
32	20	China	(FG)	Expanded	24.00	3	620	1333	(C)	3610	37	

	7			Body								
33	208	China	(FG)	Expanded Body	24.00	3	620	1333	(C)	3610	40	
34	218	China	(FG)	Expanded Body	19.00	3	700	1500	(C)	6284	74	(Piao & Qu 2012)
35	219	China	(FG)	Expanded Body	8.90	2	600	1100	(C)	959	54	(Cui & Wang 2012)
36	220	China	(FG)	Expanded Body	17.30	2	700	1400	(C)	11748	31	(Yin et al. 2017)
37	221	China	(FG)	Expanded Body	17.30	2	700	1400	(C)	9020	13	
38	222	China	(FG)	Expanded Body	17.30	2	700	1400	(C)	8994	22	
39	224	China	(FG)	Expanded Body	16.70	1	600	1400	(C)	2010	35	(Dehong et al. 2017)
40	225	China	(FG)	Expanded Body	16.70	1	600	1400	(C)	2060	38	
41	238	China	(FG)	Expanded Body	36.80	2	700	1400	(C)	7986	62	(Zhang et al. 2018)
42	239	China	(FG)	Expanded Body	36.80	2	700	1400	(C)	8007	61	
43	240	China	(FG)	Expanded Body	36.80	2	700	1400	(C)	8007	64	
44	254	Canada	(FG)	Helical	3.05	3	219	356	(C)	158	36	(Zhang 1999)
45	255	Canada	(FG)	Helical	5.18	3	219	356	(C)	182	38	
46	256	Canada	(FG)	Helical	5.18	3	219	356	(C)	193	70	
47	257	Canada	(FG)	Helical	5.18	2	219	356	(C)	216	32	
48	259	Canada	(FG)	Helical	3.05	3	219	356	(T)	155	59	
49	260	Canada	(FG)	Helical	5.18	3	219	356	(T)	220	71	

50	261	Canada	(FG)	Helical	5.18	2	219	356	(T)	221	35	
51	264	Canada	(S)	Helical	3.05	3	219	356	(C)	459	50	
52	265	Canada	(S)	Helical	5.18	3	219	356	(C)	482	68	
53	266	Canada	(S)	Helical	5.18	2	219	356	(C)	391	40	
54	267	Canada	(S)	Helical	3.05	3	219	356	(T)	196	46	
55	268	Canada	(S)	Helical	5.18	3	219	356	(T)	367	58	
56	269	Canada	(S)	Helical	5.18	2	219	356	(T)	384	50	
57	294	Brazil	(FG)	Helical	10.50	4	88.9	318	(T)	224	72	(dos Santos Filho & Cavalcanti Tsuha 2019)
58	298	Brazil	(FG)	Helical	9.00	6	88.9	331	(T)	364	78	
59	300	Brazil	(FG)	Helical	11.50	4	88.9	318	(T)	463	79	
60	302	Brazil	(FG)	Helical	13.50	4	88.9	318	(T)	501	46	
61	304	Brazil	(FG)	Helical	12.00	6	88.9	331	(T)	499	30	
62	308	Brazil	(FG)	Helical	13.50	4	101.6	318	(T)	601	36	
63	309	Brazil	(FG)	Helical	11.00	6	101.6	331	(T)	502	72	
64	311	Brazil	(FG)	Helical	13.00	6	101.6	331	(T)	599	67	
65	317	Brazil	(FG)	Helical	11.50	4	88.9	318	(T)	499	66	
66	318	Brazil	(FG)	Helical	8.00	4	101.6	318	(T)	185	80	
6	3	Bra	(FG	Helical	16.	4	101.	31	(T)	702	42	

7	33	zil	)		00		6	8				
68	338	Canada	(S)	Helical	9.30	2	244	457	(C)	1169	23	(Tappenden 2007)
69	339	Canada	(FG)	Helical	5.90	1	273	762	(C)	1023	89	
70	340	Canada	(FG)	Helical	6.00	2	273	762	(C)	1368	80	
71	341	Canada	(FG)	Helical	5.90	1	273	762	(T)	828	84	
72	342	Canada	(FG)	Helical	6.00	2	273	762	(T)	1309	98	
73	343	Canada	(S)	Helical	4.90	1	406	762	(T)	1793	50	
74	344	Canada	(FG)	Helical	7.50	1	219	400	(C)	1022	18	
75	345	Canada	(FG)	Helical	10.40	2	324	914	(C)	542	31	
76	355	Canada	(FG)	Helical	7.20	3	178	610	(C)	144	49	(Elsherbiny & El Naggar 2013)
77	358	Brazil	(FG)	Expanded Body	8.80	1	300	600	(C)	1002	67	(Monteiro et al. 2021)
78	360	Brazil	(FG)	Expanded Body	10.00	1	300	600	(C)	1206	53	
79	362	Brazil	(FG)	Expanded Body	10.00	1	250	600	(T)	980	55	
80	363	Brazil	(FG)	Expanded Body	8.00	1	250	600	(T)	630	58	

Fine-grained soil (FG) and Sand soil (S).
In loading direction, (C) is Compression load and (T) is Tensile load.
Number of helices or expanded parts (NEA).
Mean of helices or expanded parts diameter (MED).

Accepted manuscript doi:
10.1680/jgeen.23.00196

Table 2: Specifications of cases (S.D. = Standard deviation).

Parameter	Compression				Tensile			
	Max.	Min.	Mean	S.D.	Max.	Min.	Mean	S.D.
Embedment depth (m)	36.80	2.40	10.98	9.27	22.10	2.57	11.15	6.29
Number of helices or expanded parts	5	1	2	1	6	1	2	2
Shaft diameter (mm)	700.0	73.0	342.5	219.5	850.0	88.9	295.4	230.2
Mean expanded diameter (mm)	1500	254	734	444	1500	318	659	427
Max measured load (kN)	11748	46	2291	2994	9432	155	1506	2455

Table 3: Trend curves fitted to scatter data points and diagrams (TA = Toe Area; SA = Shaft Area).

Load direction	X	Brinch-Hansen 80% method (kN)	R^2	5.0% criterion (kN)	R^2	Maximum Measured load (kN)	R^2
Tensile	$Toe\ area\ (mm^2)$	$302.8e^{2E-6TA}$	0.91	$235.7e^{2E-6TA}$	0.98	$302.5e^{2E-6TA}$	0.69
	$Shaft\ area\ (mm^2)$	$325.6e^{6E-5SA}$	0.78	$0.045SA^{1.0925}$	0.90	$0.264SA^{0.92}$	0.69
Compressive	$Toe\ area\ (mm^2)$	$264.7e^{2E-06TA}$	0.75	$0.0014TA^{1.0493}$	0.35	$235.7e^{2E-6TA}$	0.98
	$Shaft\ area\ (mm^2)$	$0.15SA^{0.9563}$	0.89	$0.153SA - 17.74$	0.56	$0.045SA^{1.09}$	0.90

Table 4: Specifications of piles used for model verification.

No	ID	Location	Soil Type	Pile Type	Height	NEA	Shaft Dia. (mm)	MED	Description	Reference
1	I	Caspian Sea southwest shore - Anzali	Sand	Subasa open end	3.25	1	114	250		(Shojaei et al., 2022)
2	II	Caspian Sea southwest shore - Anzali	Sand	Subasa close end	3.25	1	114	250		
3	III	Caspian Sea southwest shore - Anzali	Sand	Self-Expanded Wing	3.25	1	114	250	Shaft Square	
4	IV	Caspian Sea southwest shore - Anzali	Sand	Self-Expanded SE	3.25	1	114	250		
5	V	Caspian Sea southeast shore - Inchebron	Loess	Helical	3	1	88.9	250	Dry installation	(Arabameri &

6	VI	Caspian Sea southeast shore - Inchebron	Loess	Helical	3	3	88.9	250	Dry installation S/D = 3	Eslami, 2021)
7	VII	Caspian Sea southeast shore - Inchebron	Loess	Helical	3	3	88.9	250	Dry installation S/D = 3	
8	VIII	Caspian Sea southeast shore - Inchebron	Loess	Helical	3	3	88.9	250	Wet installation S/D = 3	

Mean of helices or expanded parts diameter (MED).

Figure captions

Fig. 1 Illustrations of typical types of expanded piles.
Fig. 2 Examples of self-expanded piles (Shojaei et al., 2021).
Fig. 3 Examples of load-displacement curves for helical and expanded piles from the database.
Fig. 4 Frequency and distribution of occurrence of key parameters in the database: (a) Pile embedment depth; (b) Mean expanded diameter; (c) Pile shaft diameter; (d) Soil types; (e) Pile maximum load; (f) Number of helix or expanded parts.
Fig. 5 Load-displacement curves for 80 piles in the database: (a) Compression tests; (b) Tensile tests.
Fig. 6 Load versus displacement ratio for each of the cases.
Fig. 7 Distribution of used ultimate load method for database cases
Fig. 8 Load-displacement curves for different ultimate load ranges: (a) 0 to 500 kN (Compression); (b) 0 to 500 kN (Tensile); (c) 500 to 1000 kN (Compression); (d) 500 to 1000 kN (Tensile); (e) 1000 to 1500 kN (Compression); (f) 1000 to 1500 kN (Tensile); (g) Upper than 1500 kN (Compression); (h) Upper than 1500 kN (Tensile).
Fig. 9 Hyperbolic function fitting process.
Fig. 10 Normalized load-displacement curves along with the fitted hyperbolic functions.
Fig. 11 Transformed axis, illustrating normalized load and displacement: (a) Compression; (b) Tensile; with 95% prediction and C.I.
Fig. 12 Load-displacement curves for short piles.
Fig. 13 Load-displacement curves for semi-deep piles.
Fig. 14 Load-displacement curves for long piles.
Fig. 15 Ranges of initial stiffness, limit loads, and displacements at intersection point for various pile embedment depths (a) Initial stiffness range; (b) Limit load (1/a) range; (c) Displacement (b/a).
Fig. 16 Load-displacement behaviour based on the load direction (a) Tensile over compression curves; (b) Compressive over tensile curves; (c) Compressive crossed tensile curves.
Fig. 17 Effect of changes in ratio of the helices or expanded parts diameter to the shaft diameter: (a) Compression tests; (b) Tensile tests.
Fig. 18 Limit loads to maximum measured loads (MML) or ultimate load (a) ratio; (b) curves.
Fig. 19 Comparison of load-displacement behaviour from the tests on the piles and from the database prediction.

Accepted manuscript doi:
10.1680/jgeen.23.00196

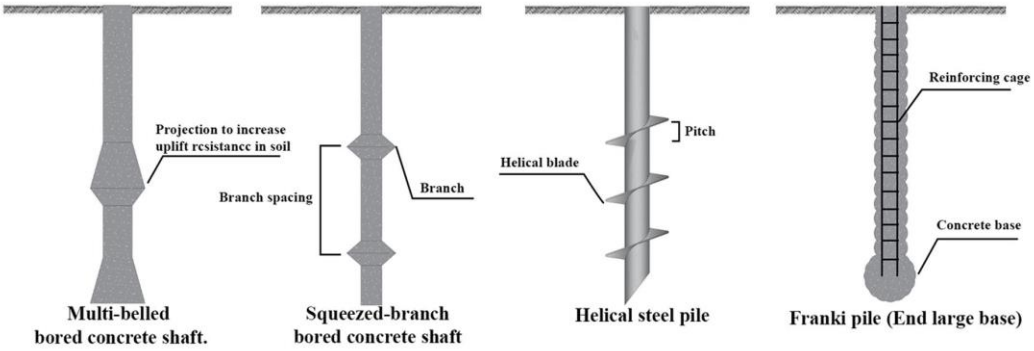

Fig 1

Accepted manuscript doi:
10.1680/jgeen.23.00196

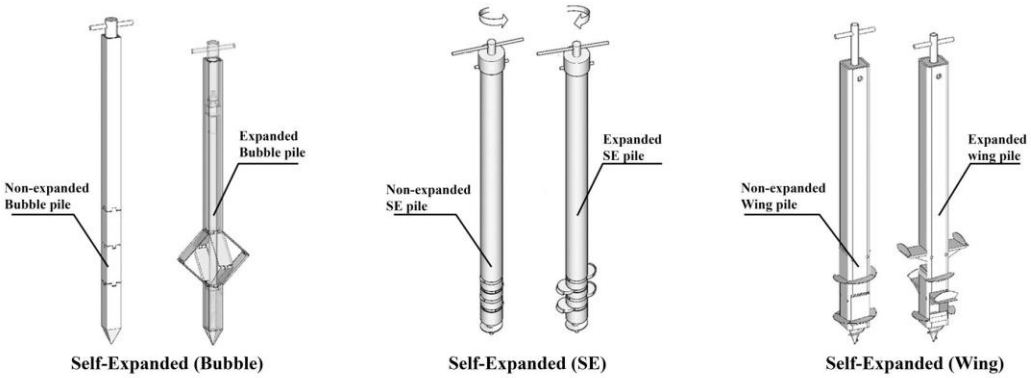

Fig 2

Accepted manuscript doi:
10.1680/jgeen.23.00196

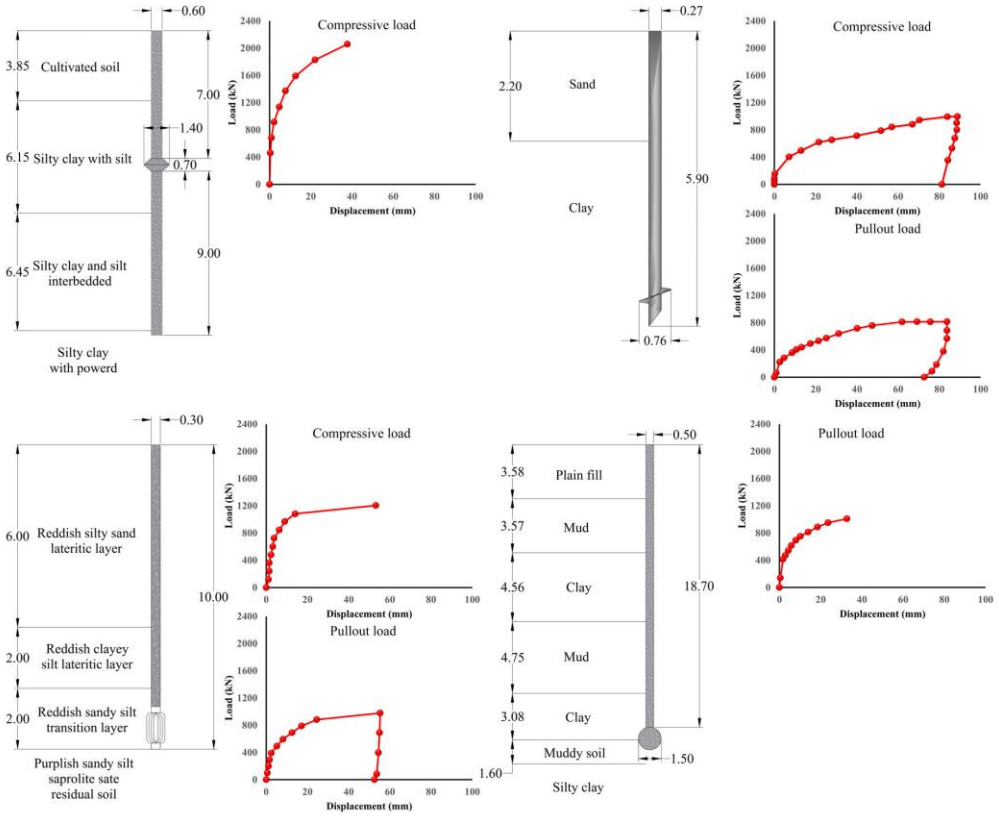

Fig 3

Accepted manuscript doi:
10.1680/jgeen.23.00196

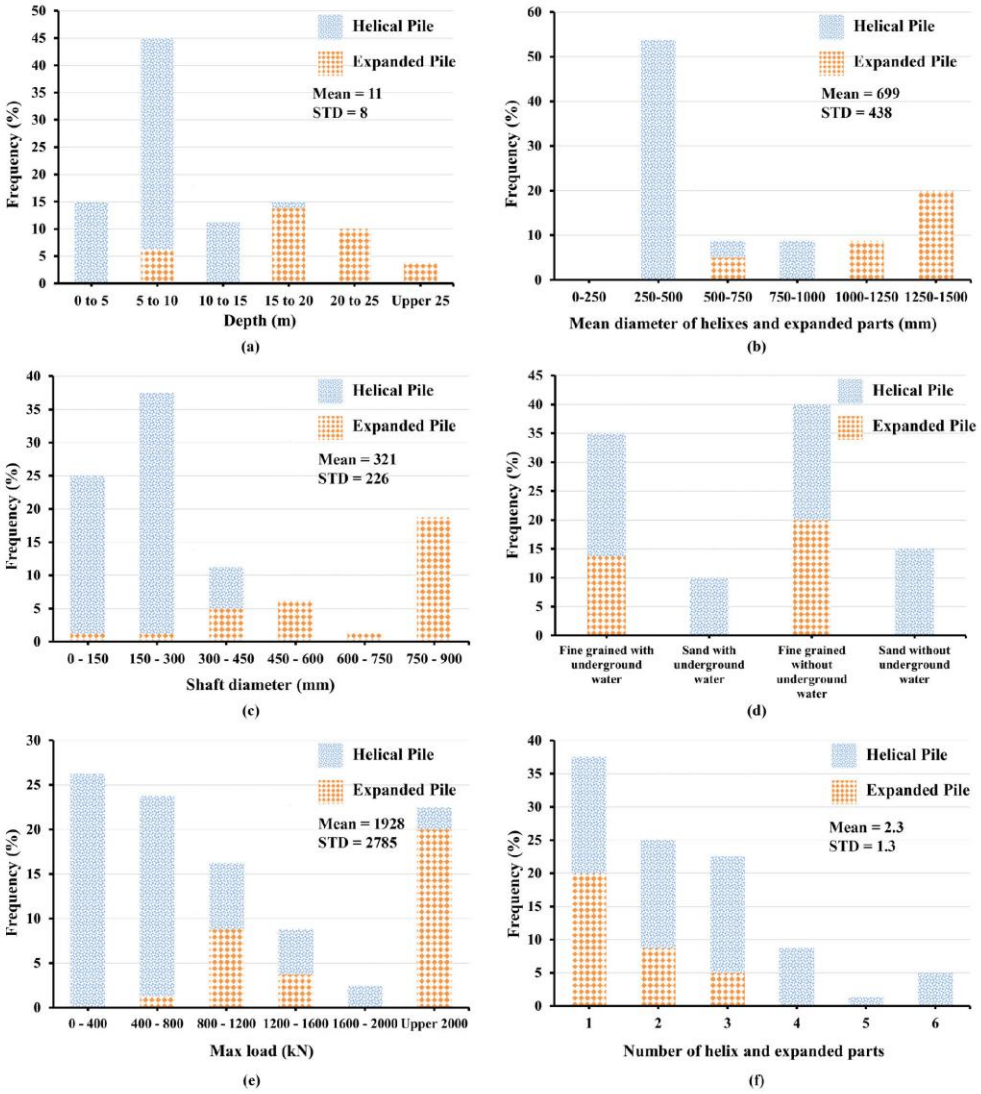

STD: standard deviation

Fig 4

Accepted manuscript doi:
10.1680/jgeen.23.00196

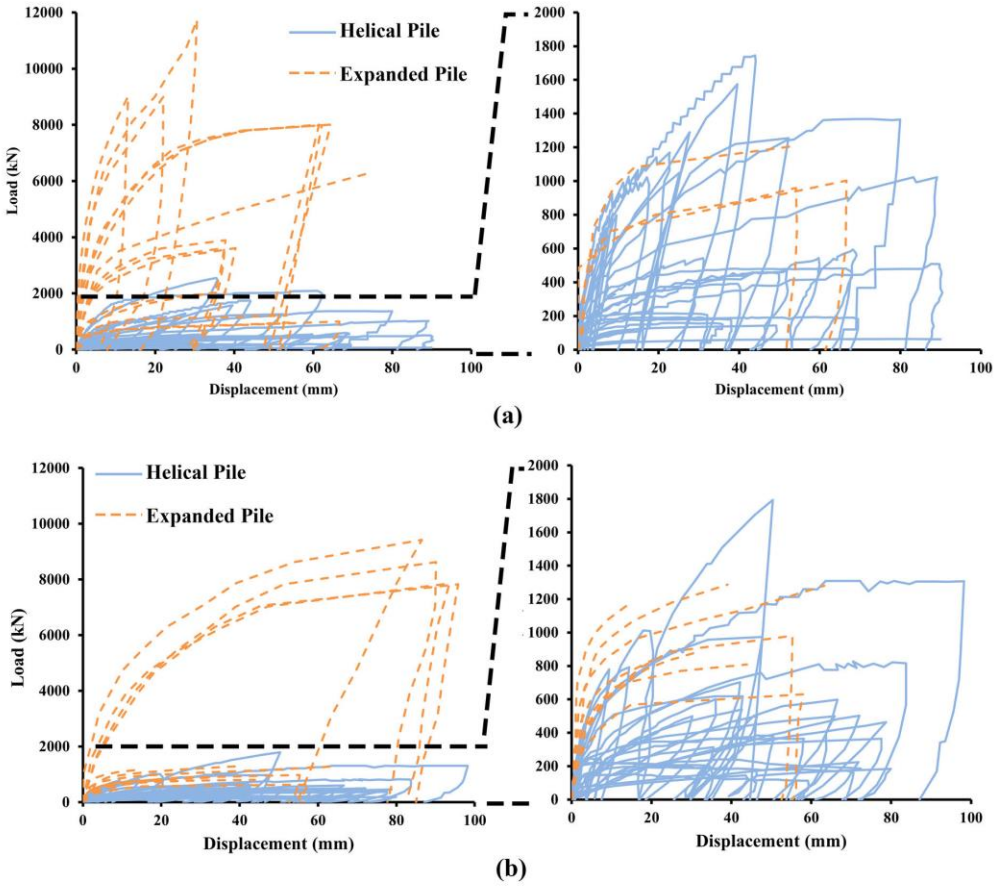

Fig 5

Accepted manuscript doi:
10.1680/jgeen.23.00196

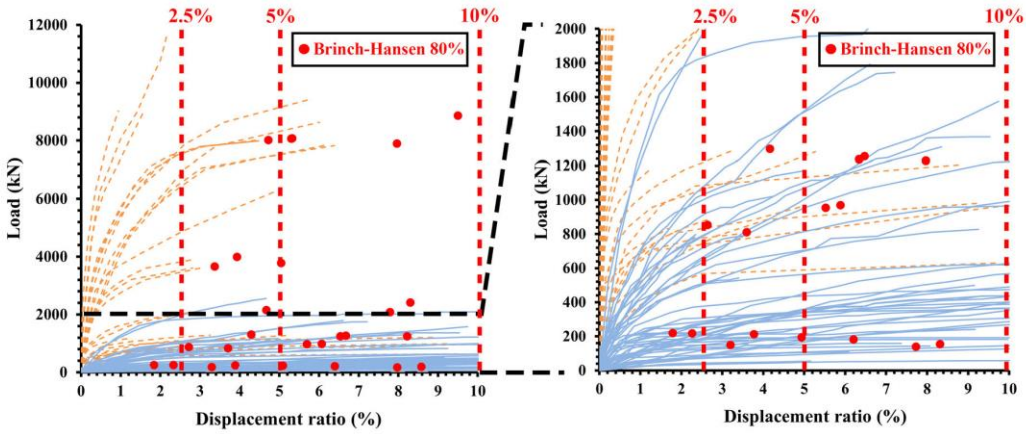

Fig 6

Accepted manuscript doi:
10.1680/jgeen.23.00196

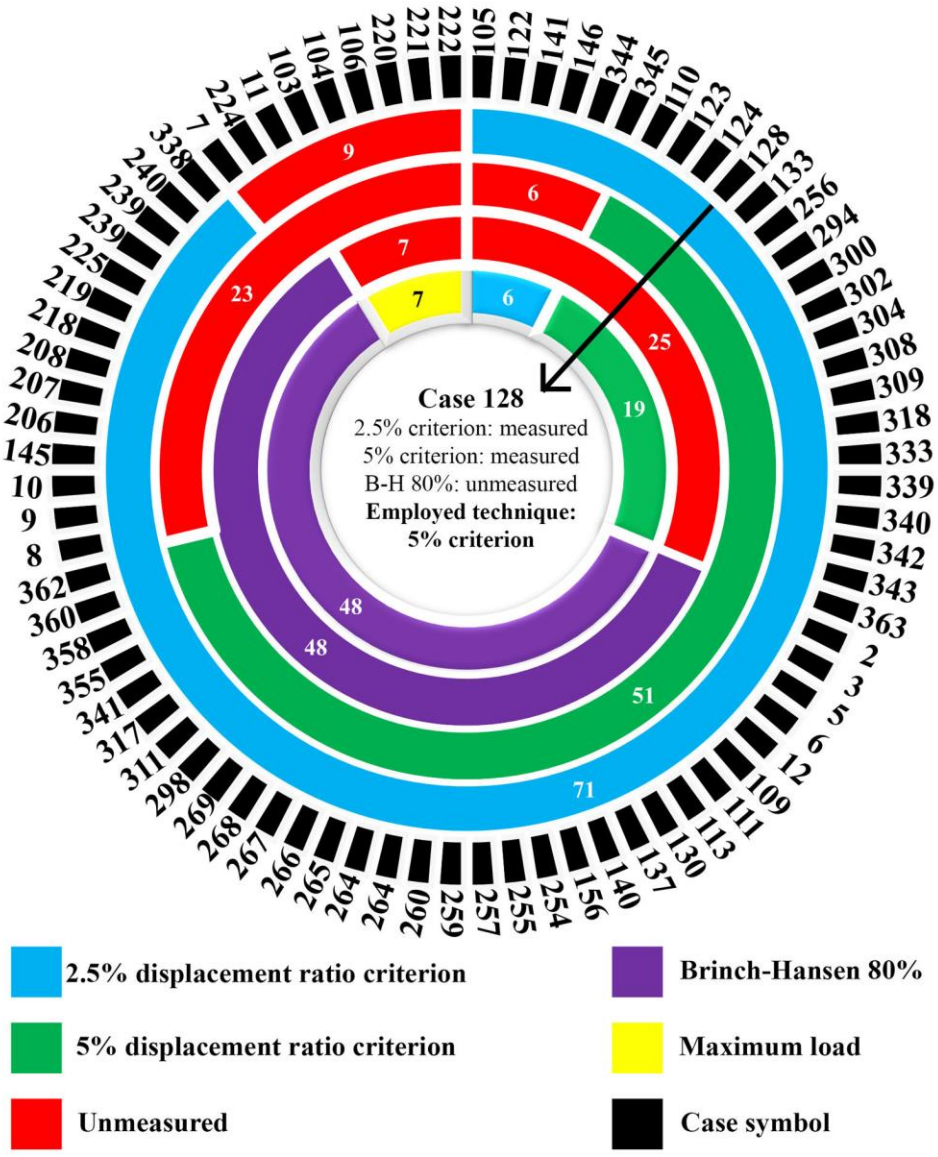

Fig 7

Accepted manuscript doi:
10.1680/jgeen.23.00196

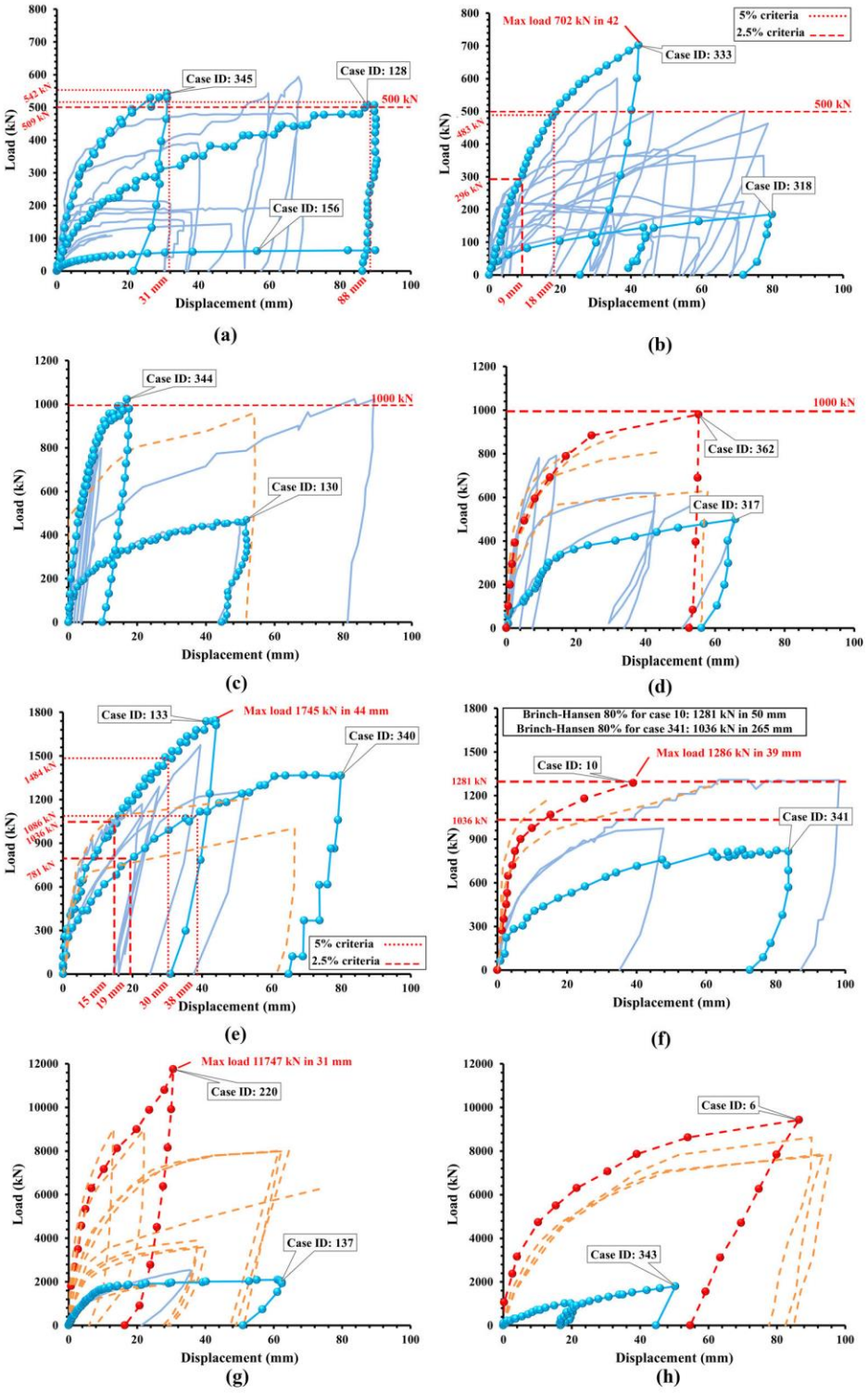

Fig 8

Accepted manuscript doi:
10.1680/jgeen.23.00196

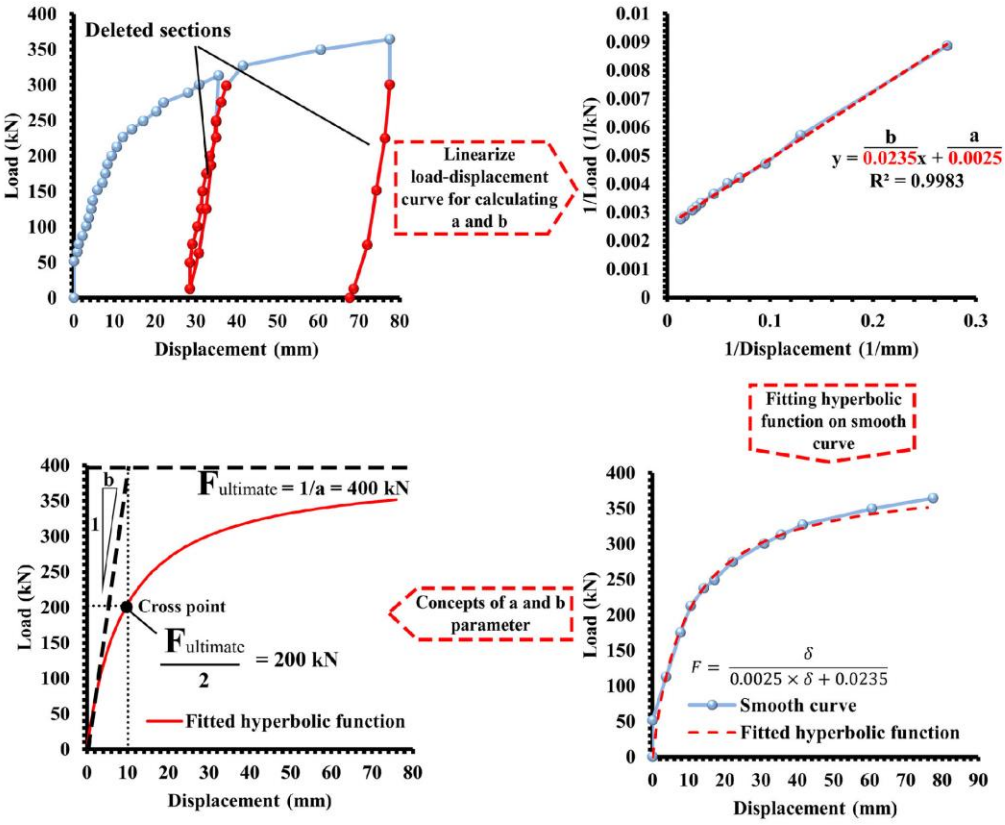

Fig 9

Accepted manuscript doi:
10.1680/jgeen.23.00196

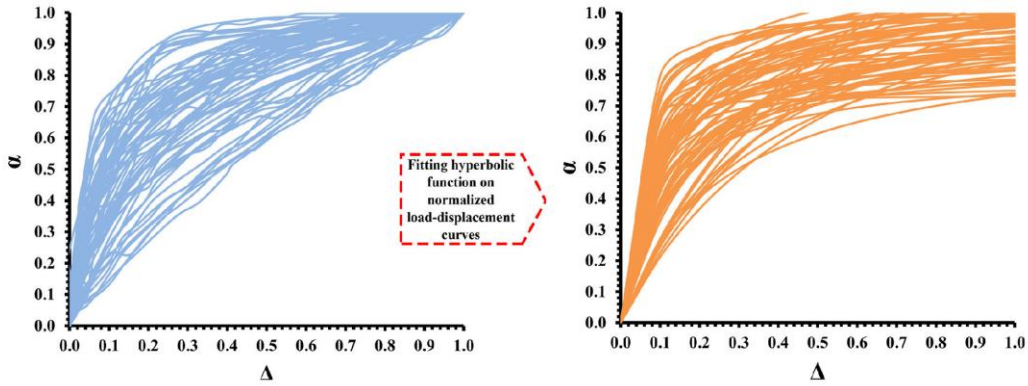

Fig 10

Accepted manuscript doi:
10.1680/jgeen.23.00196

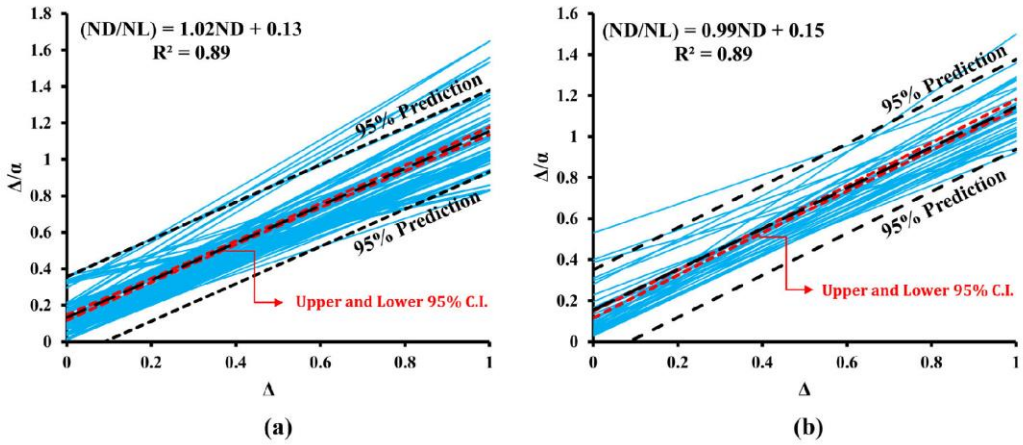

Fig 11

Accepted manuscript doi:
10.1680/jgeen.23.00196

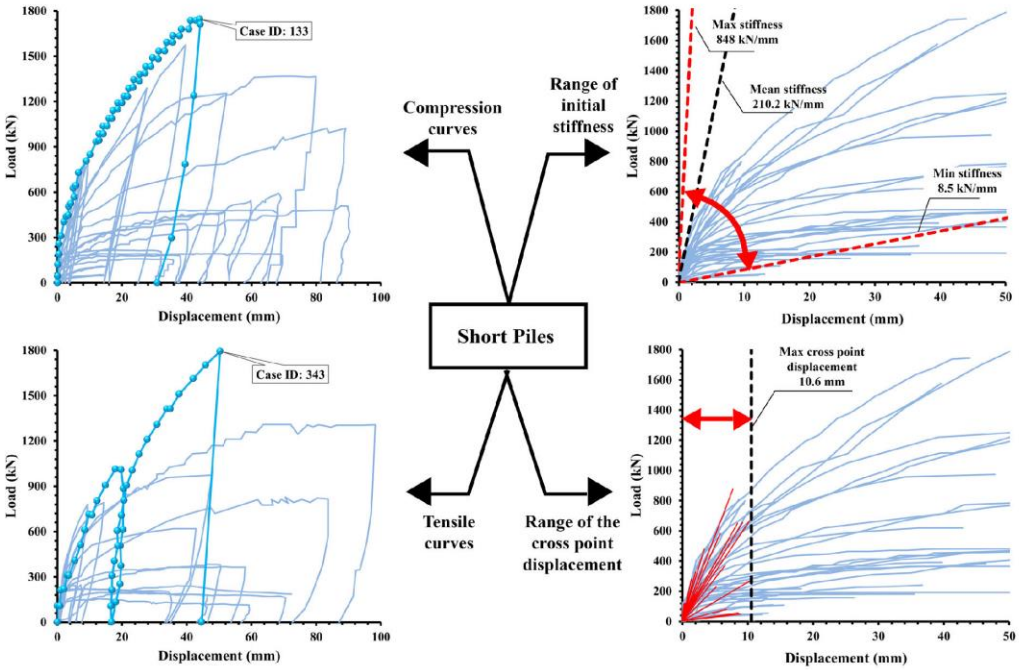

Fig 12

Accepted manuscript doi:
10.1680/jgeen.23.00196

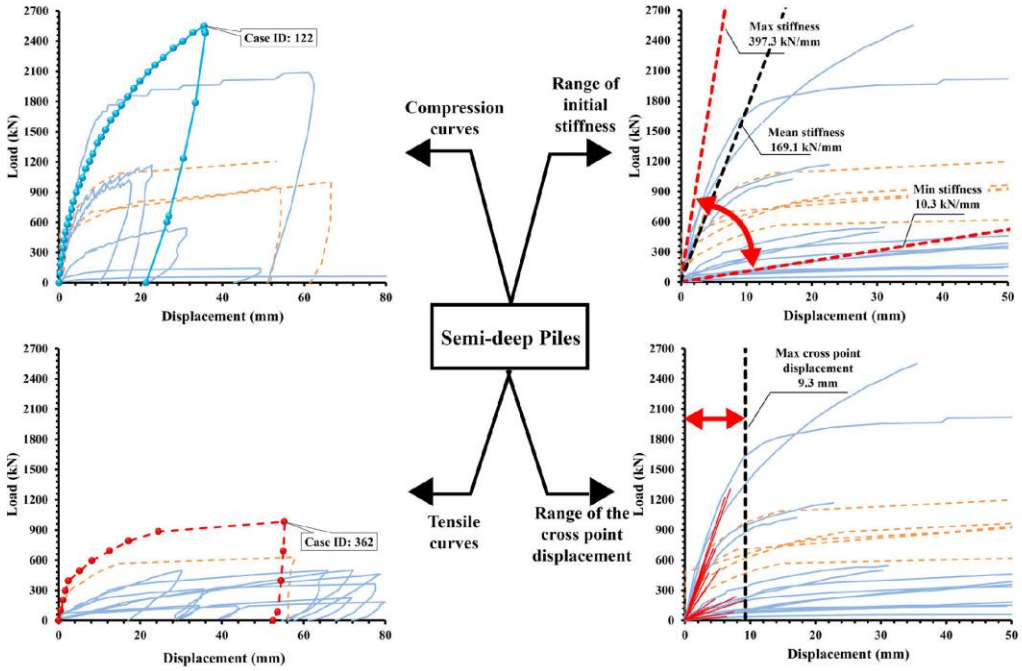

Fig 13

Accepted manuscript doi:
10.1680/jgeen.23.00196

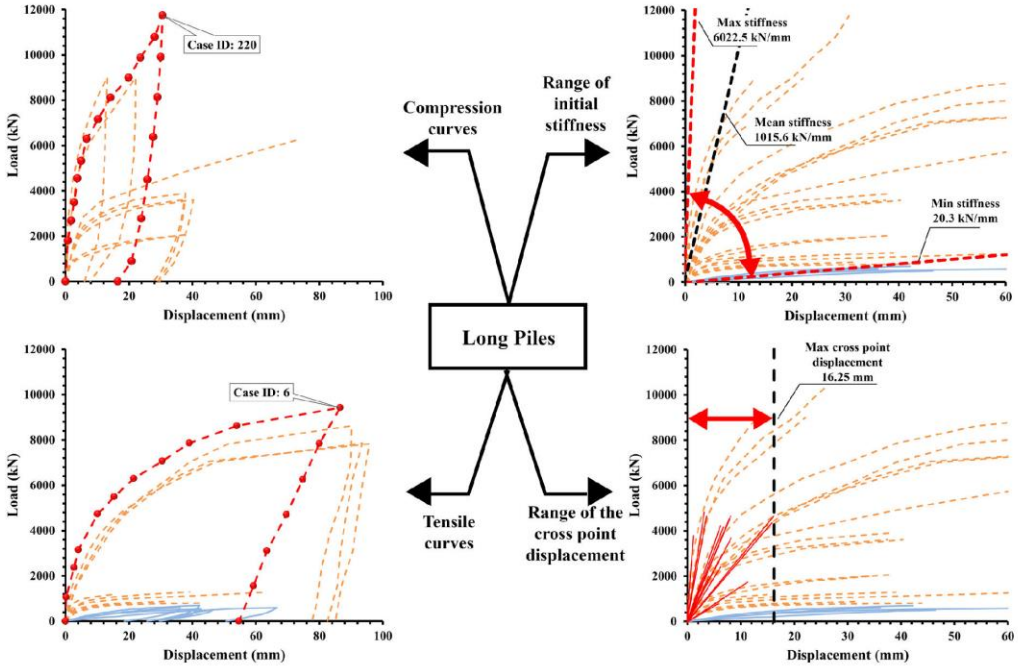

Fig 14

Accepted manuscript doi:
10.1680/jgeen.23.00196

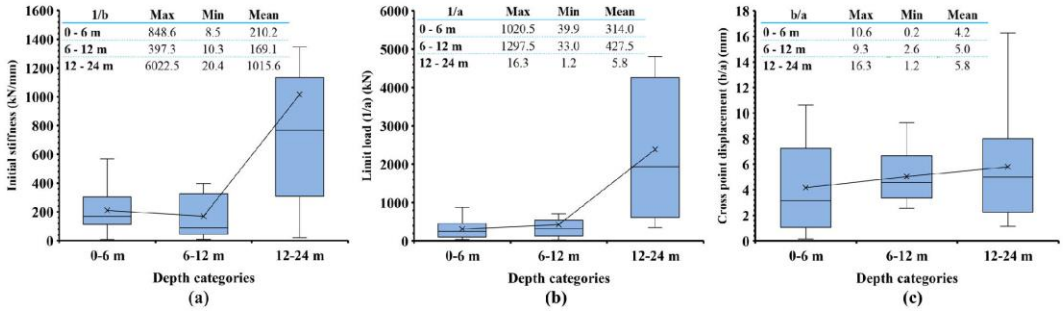

Fig 15

Accepted manuscript doi:
10.1680/jgeen.23.00196

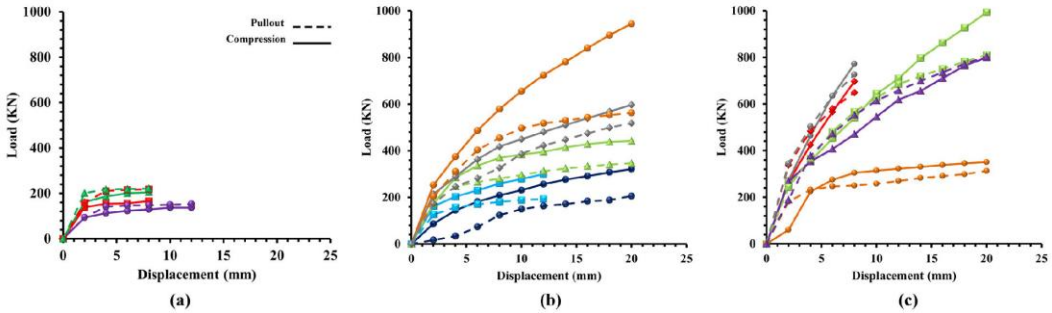

Fig 16

Accepted manuscript doi:
10.1680/jgeen.23.00196

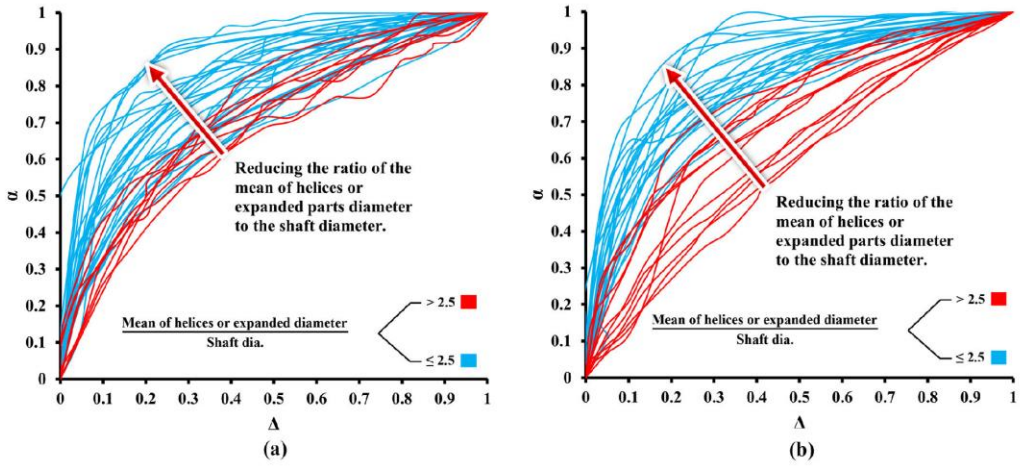

Fig 17

Accepted manuscript doi:
10.1680/jgeen.23.00196

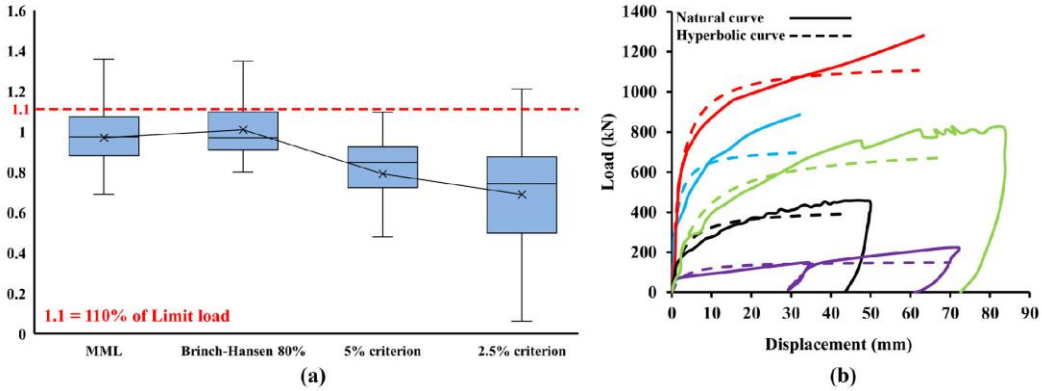

Fig 18

Accepted manuscript doi:
10.1680/jgeen.23.00196

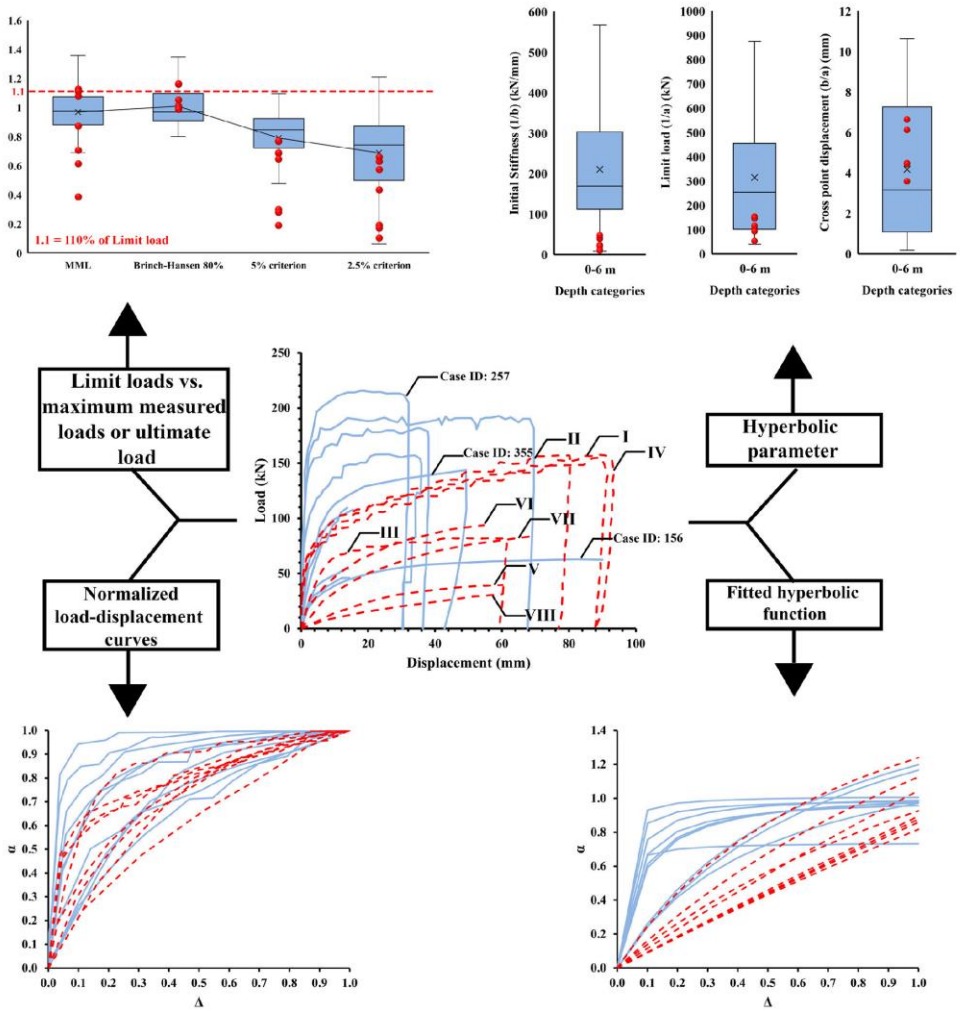

Fig 19